

Computer vision-assisted investigation of boiling heat transfer on segmented nanowires with vertical wettability

Jonggyu Lee^{1,§}, Youngjoon Suh^{1,§}, Max Kuciej², Peter Simadiris¹, Michael T. Barako^{1,3}, Yoonjin Won^{1,4,*}

¹ Department of Mechanical and Aerospace Engineering, University of California, Irvine, Irvine, CA, 92697, USA.

² Department of Material Science and Engineering, University of California, Los Angeles, Los Angeles, CA, 90095, USA

³ NG Next, Northrop Grumman Corporation, Redondo Beach, CA, 90278, USA.

⁴ Department of Electrical Engineering and Computer Science, University of California, Irvine, Irvine, CA, 92697, USA

Co-First Authors[§], and Corresponding Author^{}*

Keywords: nanowires, heterogeneous wetting, boiling, dual wettability, machine vision

This PDF file includes:

Section S1: Surface characterization

Section S2: Pool boiling experimental setup

Section S3: Bubble dynamics analysis using computer vision

Fig. S1. Cross-sectional SEM images of the nanowires

Fig. S2. Surface characterization of flat surfaces with replicated nanotextures

Fig. S3. Contact angle measurements of NW samples before and after oxidation

Fig. S4. Droplet imbibition and spreading during contact angle measurement of nanowires after oxidation

Fig. S5. Schematic illustration of experimental setup for liquid rate-of-rise test

Fig. S6. Liquid rise on Ni NWs at 10 s

Fig. S7. Liquid pathways through segmented Ni/CuO nanowire arrays

Fig. S8. Schematic of pool boiling experimental setup

Fig. S9. Independent pool boiling tests on unmodified Si surfaces

Fig. S10. Computer vision framework and model performance evaluation

Fig. S11. Model performance as a function of intersection over union (IoU) threshold

Table S1. Film characteristics for pool boiling calculations

Table S2. Summary of extracted bubble parameters and heat flux values near the ONB

Table S3. Boiling heat transfer performances when $q_{low}'' < 15 \text{ W/cm}^2$

Table S4. Boiling heat transfer performances when $q_{low}'' < 30 \text{ W/cm}^2$

Supporting information references (1-12)

Other Supporting Information for this manuscript include the following:

Movie S1. Real-time visualization of two-step wicking on a Ni/CuO NW surface.

Movie S2. Real-time tracked bubble evolution behavior.

Section S1. Surface characterization

S1.1. Cross-sectional view of fabricated nanowires

Fig. S1 shows cross-sectional morphological details of the segmented nanowires (NW) taken from a scanning electron microscope (SEM). To create NWs with dual wettability, two metals (Ni and Cu) are selected based on thermal conductivity, intrinsic contact angle, availability for electrochemical deposition, and corrosion resistance. As Ni resists corrosion, the Cu portion is selectively oxidized and decorated by CuO nanofeatures that provide enormous surface roughness and hydrophilicity, while the Ni portion remains intactly hydrophobic. The ratio of the Cu and Ni portion lengths (l_{Cu} , l_{Ni}) and average diameter are investigated by measuring and averaging the nanowire height and diameter in Fig. S1.

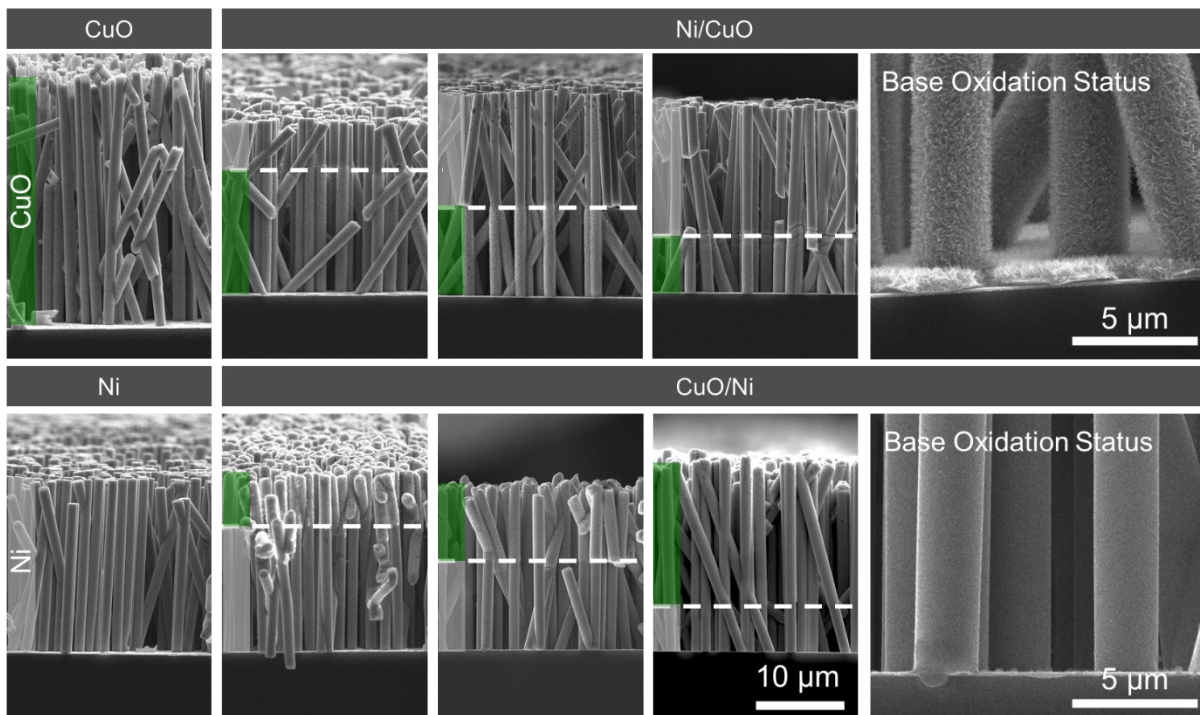


Fig. S1. Cross-sectional SEM images of the nanowires.

S1.2. Nanowire array porosity

To quantify the porosity distribution of the fabricated samples, we calculate the effective porosity of the NW by accounting for the effects of the stepwise diameter increase in the Cu segment after oxidation. The effective porosity is defined as the void fraction of the system $\phi = 1 - \varepsilon$, where ε is the NW solid fraction. The solid fraction, in turn, is calculated as $\varepsilon = \pi d^2 N / 4$, where N is the NW areal number density.¹ The number density of nanowires is $N = 0.23 \mu\text{m}^{-2}$ obtained from the top-view SEM images for all the nanowires in this study. Top-view SEM image comparison of the CuO NWs (Fig. 2i) and Ni NWs (Fig. 2j) confirm that the chemical oxidation has no noticeable effects on the NW's natural tortuosity. Therefore, the overall porosity of segmented nanowires is impacted by the ratio of the segmented Cu and Ni portions, owing to the difference in diameter between the two metal segments. Considering all these factors, the porosity of the segmented nanowire after oxidation can be calculated as follows:

$$\phi = 1 - \frac{\pi N}{4l_{tot}}(d_{Ni}^2 l_{Ni} + d_{CuO}^2 l_{CuO}) \quad (S1)$$

The calculation results are listed in the Table 1. We report an insignificant (<10%) porosity discrepancy across all NW samples used for this study. Note that the areal loss from the entanglement of the nanowires is evaluated as 0.2% from our previous study and is factored into our porosity evaluation in this study.¹

S1.3. Surface chemistry and wetting behavior

The NW's surface chemistry changes due to the selective oxidation of the Cu material. To directly compare the coupled effects of NW structures and oxidation, we first prepare plain Ni and Cu surfaces using identical substrates as shown in Fig. S2a. After oxidation, the contact angle remains relatively stable ($\Delta\theta < 8\%$) for the Ni surface while noticeably dropping by $\Delta\theta = 37\%$ for the Cu surface (Fig. S2b). The oxidation-induced contact angle drop becomes more prominent when coupled with NW geometry. By comparing Fig. S2 and Fig. S3, it becomes evident that the contact angles of the NW surfaces before oxidation are generally higher than the plain element surfaces owing to the additional roughness introduced by the NW arrays.

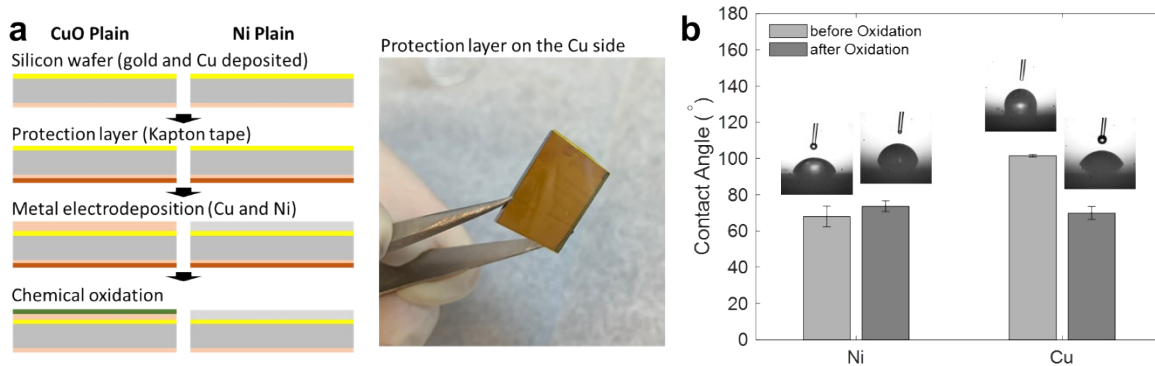


Fig. S2. Surface characterization of flat surfaces with replicated nanotextures. (a) Sample preparation of metal surfaces coated on both bottom and top of the silicon wafer. The plain and structured metal surfaces are fabricated on an Au layer using an electrodeposition method. A Cu layer is coated coated *via* E-beam evaporation on the backside of the sample to provide a metallic surface required for the soldering process. (b) Contact angle results of the plain metal surface before and after oxidation.

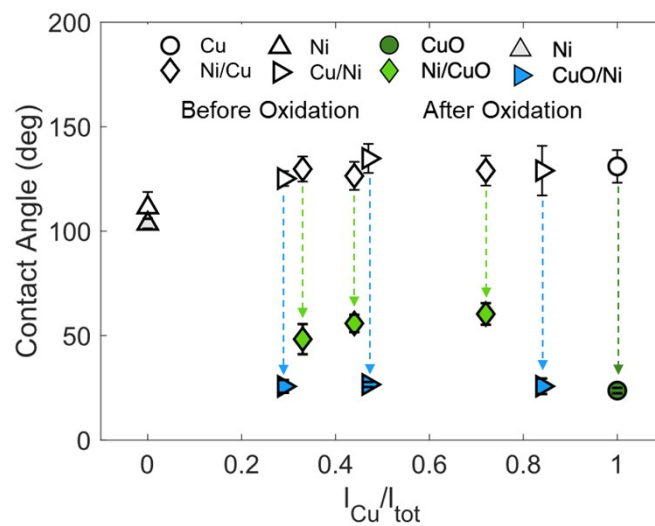


Fig. S3. Contact angle measurements of NW samples before and after oxidation.

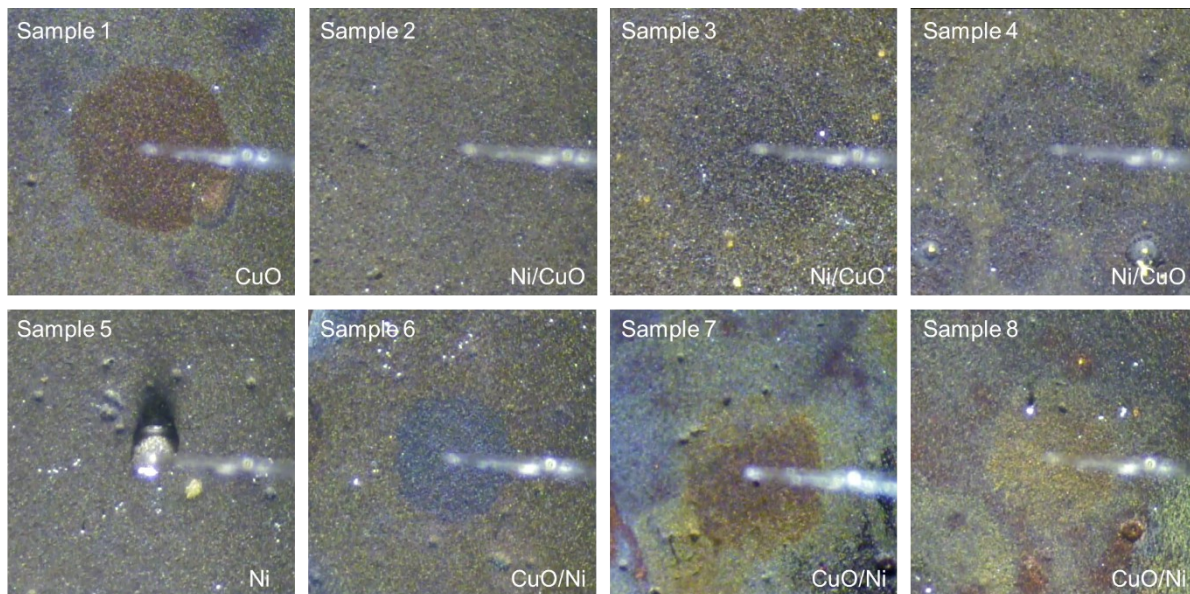


Fig. S4. Droplet imbibition and spreading during contact angle measurement of nanowires after oxidation.

S1.4. Capillary rise theory

The capillary pressure through the porous media is expressed with the Laplace-Young equation:

$$\Delta P_{cap} = \frac{2\sigma \cos \theta_s}{R_p} \quad (\text{S2})$$

where σ is the surface tension of the liquid, and R_p is the pore radius. The capillary pressure ΔP_{cap} is equivalent to the summation of the viscous friction, gravity, and evaporation during the wicking process:

$$\frac{2\sigma \cos \theta_s}{R_p} = \frac{\phi}{K} \mu h v + \frac{\dot{m}_{evp} \mu}{2d_{film} \rho K} h^2 + \rho g h \quad (\text{S3})$$

where K is permeability, μ is the liquid viscosity, d_{film} is film thickness, and ρ is the density of the liquid. As we perform the wicking test in the saturated chamber, \dot{m}_{evp} is negligible. In addition, the gravitational term becomes negligible in low wicking height (< 10 mm) condition. Eq. (S2) can then be reduced to the Lucas-Washburn equation:¹

$$h^2 = \frac{4\sigma K}{\phi \mu R_{eff}} t \quad (\text{S4})$$

S1.5. Uncertainty analysis for liquid rate-of-rise test

Capillary performance parameter. As K/R_{eff} is a function of the porosity, fluid viscosity, surface tension, wicking height, and measurement time (Eq. S4), The uncertainty of the K/R_{eff} is:

$$\frac{\Delta K/R_{eff}}{K/R_{eff}} = \sqrt{\left(\frac{\Delta\sigma}{\sigma}\right)^2 + \left(\frac{\Delta\phi}{\phi}\right)^2 + \left(\frac{\Delta\mu}{\mu}\right)^2 + \left(2\frac{\Delta h}{h}\right)^2 + \left(\frac{\Delta t}{t}\right)^2} \quad (S5)$$

Because the fluid properties change with the lab ambient temperature 298 ± 2 K, the uncertainty in the surface tension and viscosity is 0.6% and 4.4%, respectively. Furthermore, the framerate of the high-speed camera used to capture the wicking is 60 fps, resulting in an uncertainty of approximately 8.4 ms ($< 0.015\%$). Therefore, we consider that uncertainty caused by liquid properties and timeframe is negligible. Consequentially, the measurement error of the wicking height Δh causes the most overall uncertainty and is thus used for the calculation of the error of K/R_{eff} .¹

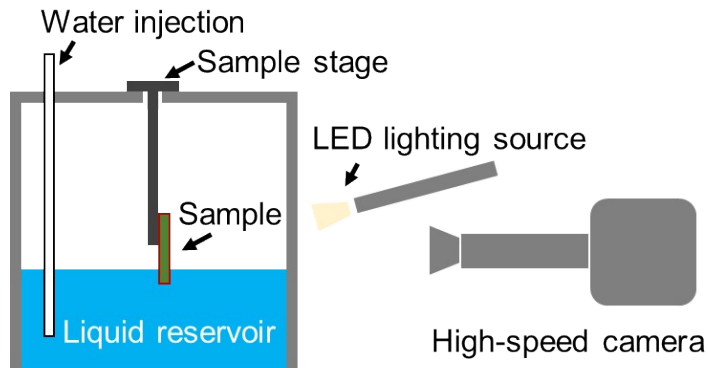


Fig. S5. Schematic illustration of experimental setup for liquid rate-of-rise test. The setup is composed of a liquid chamber, water injection system, sample stage, and CCD camera. The water is injected gradually to control water height to initiate capillary rise. The test is performed in a saturation chamber to prevent evaporation during the liquid rise.

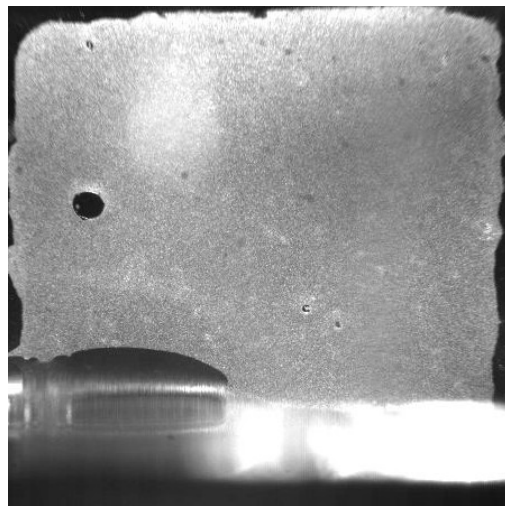


Fig. S6. Liquid rise on Ni NWs at 10 s. Capillary wicking is not observed on the Ni NWs due to the hydrophobic property. The meniscus that is formed partially on the edge of the sample might be due to the exposure of the hydrophilic Au bottom layer.

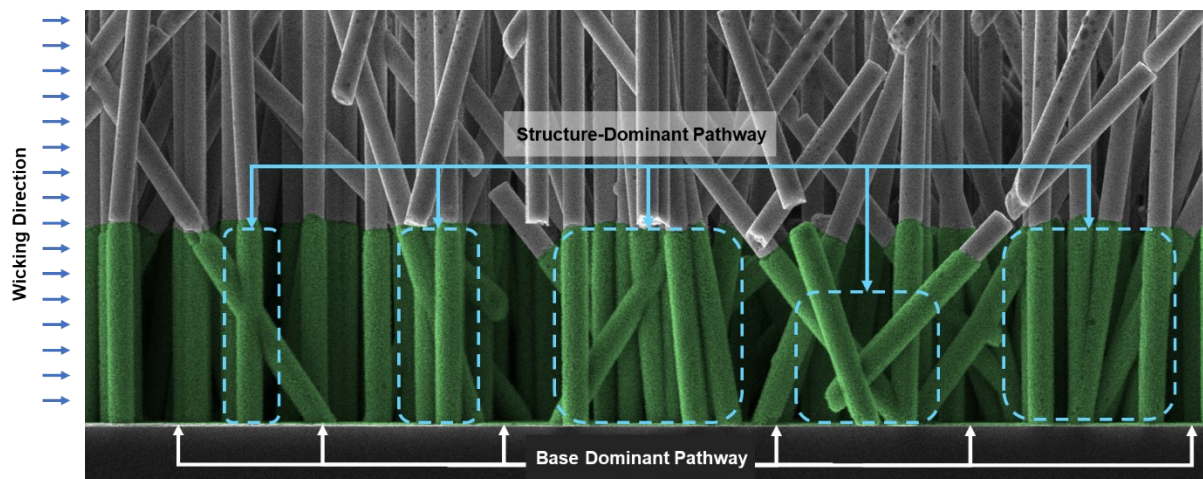


Fig. S7. Liquid pathways through segmented Ni/CuO nanowire arrays. Liquid travels in the path of least hydraulic resistance. Structure-dominant liquid pathways form in regions where NW arrays are clustered due to the reduction of effective wicking distances. When NWs are spaced far apart, the liquid primarily wicks through the hydrophilic CuO base layer. Therefore, at low CuO content, the wicking is promoted through the efficient wicking pathways through the base layer. The capillary performance reduces with increasing CuO content as structure-dominant pathways start governing the overall liquid delivery.

Section S2. Pool boiling experimental setup

S2.1. Uncertainty and repeatability analysis for pool boiling experiment

The uncertainties for pool boiling experiments are computed by using the law of propagation of uncertainty. The heat flux $q'' = k\Delta T/L$ is a function of temperature gradients, material properties, and thermocouple positions. q'' is calculated by averaging the measured q'' values obtained from thermocouples 1 – 4 as shown:

$$q'' = k \left[\frac{\left(\frac{T_1 - T_2}{L_1} \right) + \left(\frac{T_2 - T_3}{L_2} \right) + \left(\frac{T_3 - T_4}{L_3} \right)}{3} \right] \quad (S6)$$

where $T_{i=1,2,3,4}$ are the temperature readings from the four thermocouples used in the experiment, k is the thermal conductivity, and $L_{i=1,2,3}$ are the distance between thermocouples (Table S1).

By assuming that the thermal conductivity remains constant during experiments and that positional errors are minimized, the uncertainties become dictated by thermocouple readings ($U_T = \pm 0.11^\circ\text{C}$). As a result, the uncertainty of the heat flux becomes:

$$\frac{U_{q''}}{q''} = \sqrt{\left(\frac{U_T}{\Delta T_{1-2}} \right)^2 + \left(\frac{U_T}{\Delta T_{2-3}} \right)^2 + \left(\frac{U_T}{\Delta T_{3-4}} \right)^2} \quad (S7)$$

By solving for Eqn. (S8), an uncertainty of approximately 3% is calculated for the maximum heat flux. Therefore, error bars are not shown in Fig.5 and Fig. S9 for clarity.

The repeatability of the pool boiling behavior as well as the sample mounting procedure is tested by conducting an individual experiment on the unmodified bare Si surface. The acquired pool boiling and HTC curves for the tests (Fig. S9) show good repeatability.

Table S1. Film characteristics for pool boiling calculation

Symbol	Definition	Unit
q''	Heat flux	W/m ²
$T_1 - T_4$	Temperature readings from thermocouples 1 – 4	°C
$L_1 - L_4$	Distance between thermocouples	mm

Material	Subscript Notation	Thickness (nm)	Thermal Conductivity k (W/mK)
Titanium	Ti/Au	5	16
Gold	Au	50	314
Copper	Cu	1000	398
Silicon	Si	300000	130

Material	Subscript Notation	Thickness (nm)	Thermal Resistance R (m ² K/W)
Silver Paste	Sp	7.1×10^6	8.71×10^{-6}

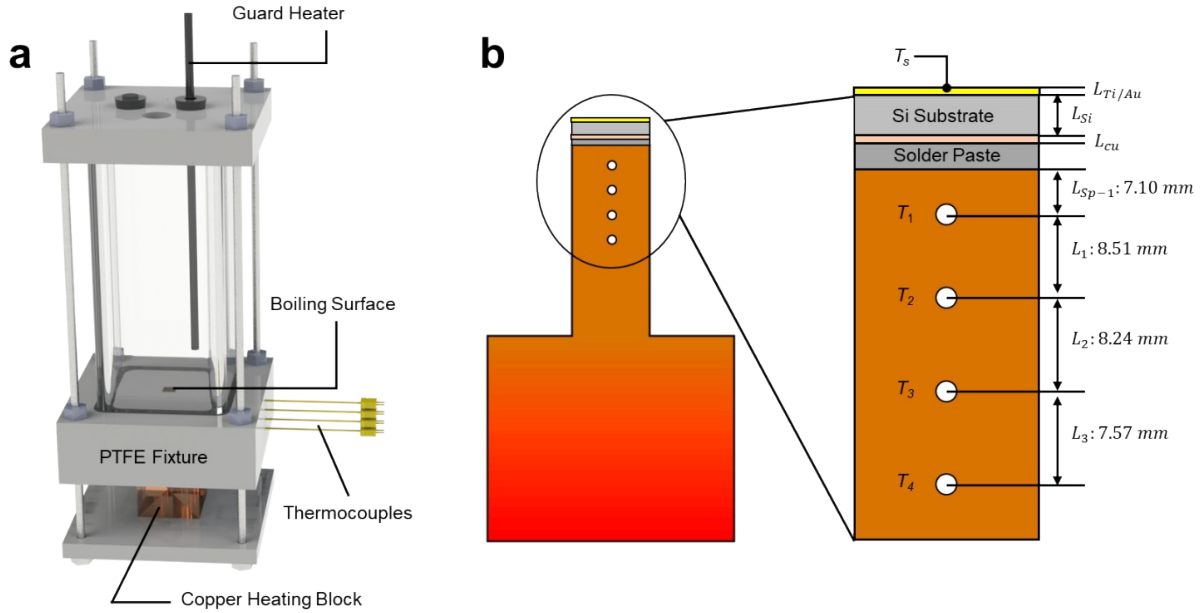


Fig. S8. Schematic of pool boiling experimental setup. (a) The pool boiling setup consists of a clear boiling chamber, PTFE fixture, a guard heater, and thermocouple-embedded copper heating block. (b) The samples are soldered onto the boiling surface as shown. The heat flux is estimated by averaging the measurements obtained from four embedded thermocouples with illustrated spacings. The copper heating block is surrounded with a glass wool insulator to minimize heat loss and promote one-dimensional heat transfer.

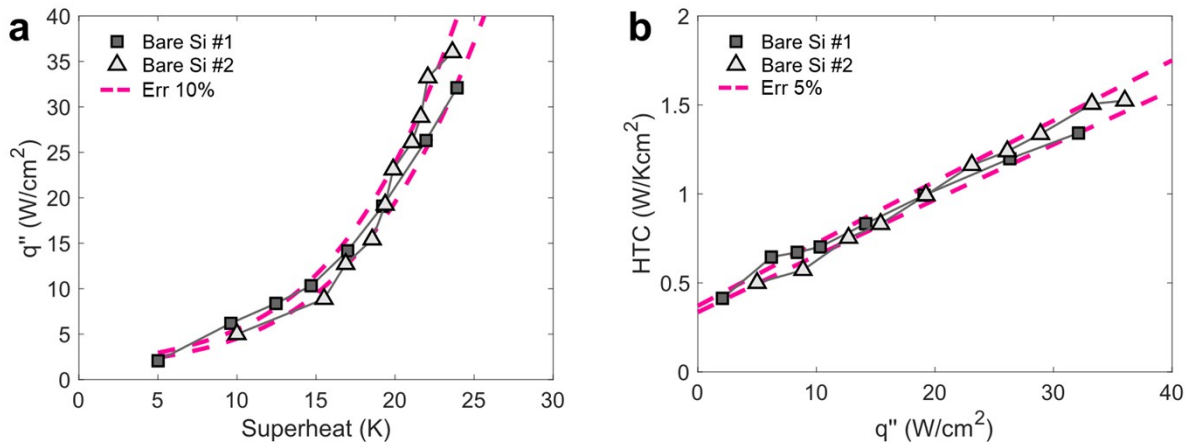


Fig. S9. Independent pool boiling tests on unmodified Si surfaces. (a) Pool boiling heat flux q'' as a function of wall superheat ($T_s - T_{sat}$), and (b) HTC as a function of q'' . Dotted lines show margin of errors from curve fitted data of the combined experiments. Error bars are not shown for clarity.

Section S3. Bubble dynamics analysis using deep learning

S3.1. Intelligent vision-based framework

Our developed framework consists of an object detection, object tracking, and data processing module to extract physical descriptors from experimentally acquired pool boiling image datasets. 1) Object detection module: As illustrated in Fig. S9a, high-resolution droplet images first pass through a custom-trained object detection module (Mask R-CNN) where droplet masks assigned with unique IDs are generated. At this stage, the model records primitive spatial features (e.g., equivalent diameter, pixel-wise area, eccentricity, orientation, solidity, and location). 2) Object tracking module: The detected masks then pass through a tracking module (TrackPy) where the IDed spatial features are used as parameters for tracking via the k-dimensional (k-d) tree algorithm. During the bubble tracking process, potential errors are manually identified and corrected using a documented graphical user interface (GUI). The model accuracy from the object detection/tracking is validated by testing evaluation metrics such as recall, precision, accuracy, F1-score, mean average pixel error (MAPE), and occlusion-induced errors, see Section S3.2 for details. 3) Data processing module: The datasets are finally post-processed to extract higher-level features (e.g., departure bubble diameter D_b , departure frequency f_b , and effective nucleation site density N_b) and visualized via Matlab.

S3.2. Model evaluation

To validate our model prediction performance, we develop a MATLAB script that checks if the predicted dataset pixels correspond with the labeled data (i.e., ground truth (GT)). A positive condition is when a model detects an instance that matches the GT and is counted as a true positive (TP). By contrast, a false positive (FP) instance is counted when the model predicts a nonexisting object. Similarly, true negative (TN) situations when the model correctly predicts no existing instances, and false negative (FN) counts instances when an existing object is undetected. These conditions are summed across the dataset and used to determine the standard performance metrics of an object detection model:^{2,3}

$$Accuracy = \frac{TP + TN}{TP + TN + FN + FP} \quad (S8)$$

$$Recall = \frac{TP}{TP + FN} \quad (S9)$$

$$Precision = \frac{TP}{TP + FP} \quad (S10)$$

$$F1\ Score = 2 * \frac{(Precision * Recall)}{(Precision + Recall)} \quad (S11)$$

For a more comprehensive analysis, we determine the positive and negative conditions on a pixel-based level (Fig. S10c). When using conventional methods based on IoU thresholds, the model retains its performance >90% until very tight IoU thresholds >0.9 are used (Fig. S11). Furthermore, we define a new performance metrics called the mean average percentage error (MAPE) for more

detailed evaluations of the model prediction accuracies at the pixel-level. For this, a pixel-wise error (PE) is calculated by subtracting the ground truth binary mask from the predicted binary mask (PBM), then dividing by the ground truth. This results in the true negatives being removed from the binary matrix, leaving only true positive, false positive, and false negative pixels. MAPE is then calculated as:

$$MAPE = \frac{1}{n} \sum_{i=1}^n |PE| \times 100 = \frac{1}{n} \sum_{i=1}^n \left| \frac{GT - PBM}{GT} \right| \times 100 \quad (S12)$$

Our framework displays striking performance (>90%) on all metrics (Fig. S9b). To characterize occlusion-induced errors, we manually compare a dataset consisting of >200 random labelled images with model predictions and solely estimate occlusion-induced errors of surface bubbles by assuming spherical morphologies. We report a maximum occlusion-induced error of 4.6%.

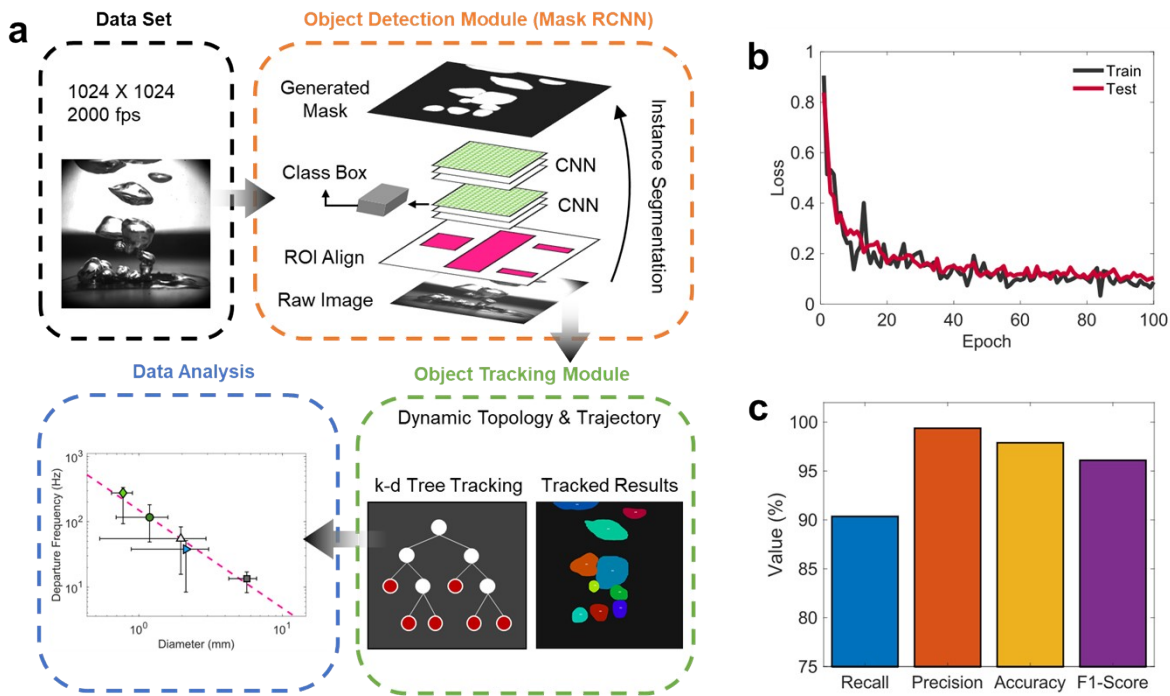


Fig. S10. Computer vision framework and model performance evaluation. (a) The object detection module uses high-speed, high-resolution images as an input dataset. Next, the images are passed through an object detection module (Mask R-CNN) where bubbles are automatically detected and labelled with pixel-wise masks. The masks are then linked together with respect to time through k-dimensional tree algorithms in the tracking module. Finally, the tracked results are post-processed in the data analysis module for visualization. (b) Mask R-CNN model learning curves show an exponential decaying trend. (c) The model performs exceptionally well on all traditional object detection evaluation metrics.

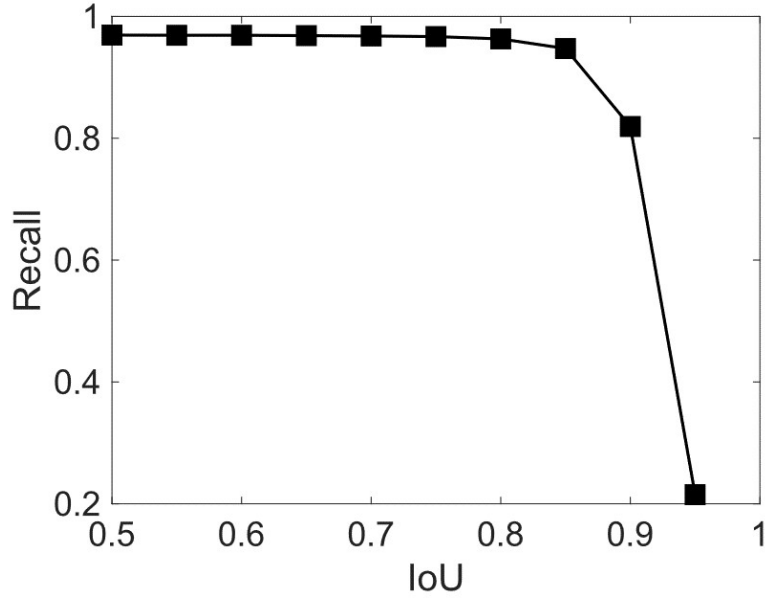


Fig. S11. Model performance as a function of intersection over union (IoU) threshold.

S3.3. Mechanistic pool boiling models and detection algorithms

The boiling heat flux released from the surface q_{tot}'' is partitioned by the three principle components, namely, natural convection q_{nc}'' outside of the bubble-influenced domain (i.e., area of influence A_{inf}), transient conduction q_{fc}'' over the area of influence, and evaporative heat transfer q_{ev}'' during phase change as follows:^{4,12}

$$q_{tot}'' = q_{nc}'' + q_{fc}'' + q_{ev}'' \quad (S13)$$

$$q_{nc}'' = \left(1 - N_b \frac{\pi D_b^2}{4}\right) h_c \Delta T \quad (S14)$$

$$q_{fc}'' = \frac{1}{2} [D_b^2 N_b (\sqrt{\pi k \rho c f_b})] \Delta T \quad (S15)$$

$$q_{ev}'' = N_b f_b \left(\frac{\pi}{6} D_b^3\right) \rho_v h_{fg} \quad (S16)$$

where N_b is the effective nucleation site density, D_b is the departure diameter, h_c is the average convective heat transfer coefficient (HTC) outside of the A_{inf} , ΔT is the superheat, and ρ is the density of the liquid, c is the heat capacity, f_b is the departure frequency and h_{fg} is the latent heat of evaporation. We note that h_c remains experimentally undefined because the convective heat transfer varies depending on the surrounding bubble nucleation and departure behaviors. Therefore, we suspect that h_c will be a function of the experimentally measured HTC and assume $h_c \approx 0.5h_{exp}$, where h_{exp} is the experimentally measured HTC.

In order to characterize the key boiling parameters, we develop custom algorithms to process spatiotemporal features with respect to the boiling surface. Bubble departure (BD) events are detected by comparing the bottom bounding box's relative position to the surface: $BD = IF(bbox_{bot,1} < y) \text{ AND } IF(bbox_{bot,2} > y)$, where $bbox_{bot,t}$ is the bottom bounding box coordinate at time t and y is the pixel value corresponding to the boiling surface. The departure frequency $f_b = 1/t_g$ is measured as a function of the bubble growth time t_g , which characterizes the time between bubble nucleation and departure. While classical theories include an additional time period, namely the waiting time t_w , which characterizes the time between bubble nucleation and departure, optical measurements confirm that $t_w \approx 0$ even at ONB. Please see Movie S2 for semi real-time mask predictions for all surfaces, where bubbles form immediately after departure.

$$N_b = \left(\frac{1}{Z} \sum_{j=1}^Z x_j \right) / A_s$$

Lastly, the effective nucleation site density is estimated as $N_b = \left(\frac{1}{Z} \sum_{j=1}^Z x_j \right) / A_s$, where x is the number of bubbles on the surface at time j , Z is the total number of timesteps, and A_s is the projected boiling surface area. To test our model's prediction validity, we compare the total theoretical heat flux q_{th} calculated from heat partitioning analysis Eq. S13-16 with experimental heat flux q_{exp} values (Table S2), showing reasonable mean error of ~13%.

Table S2. Summary of extracted bubble parameters and heat flux values near the ONB.

Surface Type	D_b (mm)	N_b (1/cm ²)	f_b (Hz)	q_{exp} (W/cm ²)	q_{th} (W/cm ²)
Si Plain	5.64	2.1	13.45	10.32	11.23
CuO NWs	1.18	4.48	116.79	5.9	4.32
Ni/CuO NWs	0.77	4.79	275.45	3.75	3.74
Ni NWs	1.95	5.84	55	12.11	8.41
CuO/Ni NWs	2.12	5	37.95	4.87	4.93

S3.4. The low heat flux region q''_{low}

The low heat flux region is defined as a pool boiling range that the bubble dynamics at ONB could represent. Although the range defined in the current study $q'' < 20 \text{ W/cm}^2$ is based on observation of bubble morphologies during pool boiling experiments, the definition remains unclear. However, because the boiling curve is relatively linear after ONB, we show in Table S3 and Table S4 that the conclusions mentioned in this work does not change for heat fluxes up to 30 W/cm^2 , where we can safely assume that bubble characteristics differ from ONB.

Table S3. Boiling heat transfer performances when $q''_{low} < 15 \text{ W/cm}^2$.

Surface Type	l_{cu}/l_{tot}	\bar{h} ($\text{W/cm}^2\text{K}$)	\bar{h}_{low} ($\text{W/cm}^2\text{K}$)	CHF (W/cm^2)	χ	ψ
Si Plain	N/A	1.09	0.72	32.1	1	1
CuO NWs	1	3.47	0.96	128.08	1.32	3.9
Ni/CuO NWs	0.44	3	1.20	122.93	1.66	3.82
Ni NWs	0	1.73	1.70	79.25	2.34	2.46
CuO/Ni NWs	0.47	2.39	0.84	105.93	1.15	3.3

Table S4. Boiling heat transfer performances when $q''_{low} < 30 \text{ W/cm}^2$.

Surface Type	l_{cu}/l_{tot}	\bar{h} ($\text{W/cm}^2\text{K}$)	\bar{h}_{low} ($\text{W/cm}^2\text{K}$)	CHF (W/cm^2)	χ	ψ
Si Plain	N/A	1.09	0.76	32.1	1	1
CuO NWs	1	3.47	1.45	128.08	1.91	3.9
Ni/CuO NWs	0.44	3	1.54	122.93	2.02	3.82
Ni NWs	0	1.73	1.71	79.25	2.24	2.46
CuO/Ni NWs	0.47	2.39	1.33	105.93	1.75	3.3

References

1. Lee, J.; Suh, Y.; Dubey, P. P.; Barako, M. T.; Won, Y., Capillary Wicking in Hierarchically Textured Copper Nanowire Arrays. *Acs Appl Mater Inter* **2019**, *11* (1), 1546-1554.
2. Visa, S.; Ramsay, B.; Ralescu, A. L.; Van Der Knaap, E., Confusion Matrix-based Feature Selection. *MAICS* **2011**, *710*, 120-127.
3. Powers, D. M., Evaluation: from precision, recall and F-measure to ROC, informedness, markedness and correlation. *arXiv preprint arXiv:2010.16061* **2020**.
4. Benjamin, R.; Balakrishnan, A., Nucleate pool boiling heat transfer of pure liquids at low to moderate heat fluxes. *Int J Heat Mass Tran* **1996**, *39* (12), 2495-2504.
5. Gerardi, C.; Buongiorno, J.; Hu, L. W.; McKrell, T., Study of bubble growth in water pool boiling through synchronized, infrared thermometry and high-speed video. *Int J Heat Mass Tran* **2010**, *53* (19-20), 4185-4192.
6. Graham, R. W.; Hendricks, R. C., Assessment of convection, conduction, and evaporation in nucleate boiling. **1967**.
7. Han, C.-Y. The mechanism of heat transfer in nucleate pool boiling. Massachusetts Institute of Technology, 1962.
8. Judd, R.; Hwang, K., A comprehensive model for nucleate pool boiling heat transfer including microlayer evaporation. **1976**.
9. Kim, M.; Kim, S. J., A mechanistic model for nucleate pool boiling including the effect of bubble coalescence on area fractions. *Int J Heat Mass Tran* **2020**, *163*.
10. Kim, S. H.; Lee, G. C.; Kang, J. Y.; Moriyama, K.; Park, H. S.; Kim, M. H., Heat flux partitioning analysis of pool boiling surface using infrared visualization. *Int J Heat Mass Tran* **2016**, *102*, 756-765.
11. Mikic, B.; Rohsenow, W., A new correlation of pool-boiling data including the effect of heating surface characteristics. **1969**.
12. Podowski, M. Z.; Alajbegovic, A.; Kurul, N.; Drew, D.; Lahey Jr, R. *Mechanistic modeling of CHF in forced-convection subcooled boiling*; Knolls Atomic Power Lab., Schenectady, NY (United States): 1997.